JMEPEG (2021) 30:6618–6629
https://doi.org/10.1007/s11665-021-05936-5

1059-9495/$19.00

Effects of Secondary-Phase Formation on the Electrochemical Performance of a Wire Arc Additive Manufactured 420 Martensitic Stainless Steel under Different Heat Treatment Conditions

Salar Salahi, Mahya Ghaffari, Alireza Vahedi Nemani, and Ali Nasiri

Submitted: 18 December 2020 / Revised: 30 April 2021 / Accepted: 22 May 2021 / Published online: 1 June 2021

This study aims to investigate the effects of annealing, quenching, and tempering (Q&T) heat treatments on the microstructure, crystallographic orientation, and electrochemical performance of a wall shaped 420 martensitic stainless steel part fabricated by wire arc additive manufacturing technology. The formation of a martensitic matrix with delta ferrite in the as-printed sample, islands of spherical chromium carbides embedded in a ferritic matrix in annealed sample, and intergranular chromium-rich carbides along the primary austenite grain boundaries in addition to intra-lath Fe-rich carbides in the quenching and tempering heat treated sample were detected. To characterize the corrosion performance of the fabricated samples, open circuit potential, potentiodynamic polarization, and electrochemical impedance spectroscopy tests were performed on all samples in aerated 3.5 wt.% NaCl electrolyte at room temperature. The corrosion morphology of the as-printed sample was characterized by localized corrosion attacks adjacent to the delta ferrite phase, while severe pitting occurred in the annealed sample due to the high susceptibility of ferritic matrix-carbide interface to pitting. In contrast to the as-printed and annealed sample, the electrochemical performance of the quenched and subsequently tempered samples was found to be significantly improved, ascribed to elimination of the chromium depleted regions adjacent to the delta ferrite phase, and enhanced protectiveness of the passive film on the alloy's surface.

Keywords 420 martensitic stainless steel, corrosion, heat treatment, wire arc additive manufacturing

1. Introduction

Martensitic stainless steels (MSSs) are broadly used in automotive, aerospace, medical, and marine industries due to their excellent combination of mechanical properties and corrosion performance (Ref 1). Unlike the ferritic and austenitic stainless steels, both mechanical and corrosion performance of the MSSs can be controlled by applying proper heat treatments, leading to their expanded demands for structural applications in harsher environments (Ref 2). Most commercial sheets of MSSs are available in the soft annealed condition with islands of spherical carbides embedded in a ferritic matrix, possessing high ductility and relatively lower strength, leading to their outstanding formability (Ref 3). MSSs can also be heat treated through a quenching and tempering (Q&T) cycle, in which newly-precipitated carbides form in a martensitic matrix, resulting in a higher hardness and strength (Ref 4, 5). Among all MSSs, 420 MSS with 13 wt.% chromium is commonly used for plastic molding applications, where sufficient corrosion and wear resistance is required (Ref 6). Conventional manufacturing techniques, such as forming and casting, have been used for the fabrication of 420 MSS, while several in-service defects, including edge deterioration, diggings, and dents, have been reported for dies fabricated through aforementioned techniques (Ref 6). Recently, additive manufacturing (AM) technology has been adopted for the fabrication of 420 MSS with improved mechanical properties and minimum process-induced defects (Ref 1, 7). In a recent study, Alam et al. (Ref 1) implemented a laser-based AM technique for the fabrication of 420 MSS and reported comparable mechanical properties for the fabricated part relative to its conventionally fabricated counterpart.

Considering the recent COVID-19 outbreak and its impact on the supply chain for many industries, AM technology is suggesting promising on-site production engineering routes for the post-COVID-19 era, especially for the manufacturing sectors (Ref 8). In general, due to the layer-by-layer construction fashion and other unique process aspects, metal AM can facilitate building complex parts in a timely manner with less material waste than traditional metal manufacturing methods (Ref 9). As one of the fastest evolving metal AM technologies, wire arc additive manufacturing (WAAM) technology implements an electric arc or plasma as the heat source to fabricate

This invited article is part of a special topical focus in the *Journal of Materials Engineering and Performance* on Additive Manufacturing. The issue was organized by Dr. William Frazier, Pilgrim Consulting, LLC; Mr. Rick Russell, NASA; Dr. Yan Lu, NIST; Dr. Brandon D. Ribic, America Makes; and Caroline Vail, NSWC Carderock.

Salar Salahi, Faculty of Engineering and Applied Science, Memorial University of Newfoundland, St. John's, Canada; **Mahya Ghaffari** and **Alireza Vahedi Nemani**, Department of Mechanical Engineering, Dalhousie University, Halifax, NS B3H 4R2, Canada; and **Ali Nasiri**, Faculty of Engineering and Applied Science, Memorial University of Newfoundland, St. John's, Canada; and Department of Mechanical Engineering, Dalhousie University, Halifax, NS B3H 4R2, Canada. Contact e-mail: ssalahi@mun.ca.

medium to large-scale metal parts using a continuous wire as the feedstock material (Ref 10–12). In the authors' previous works (Ref 13, 14), the fabrication feasibility of 420 MSS parts using the WAAM technique and the preliminary mechanical properties and corrosion performance of the alloy in as-printed condition were reported. Rapid solidification and complex heating and cooling cycles associated with the WAAM process lead to the formation of a non-homogeneous microstructure containing non-equilibrium micro-constituents (Ref 6). The presence of secondary non-equilibrium micro-constituents can adversely impact the corrosion performance of the as-printed samples (Ref 14). Hence, developing a systematic post-printing heat treatment cycle is required to eliminate the formation of unfavorable micro-constituents and enhance the mechanical and corrosion performance of the WAAM part. Furthermore, the variation of crystallographic orientation (texture) during post-printing heat treatment can also contribute to the overall corrosion resistance of the alloy either by formation of a preferential texture during the heat treatment process or altering the misorientation nature of grain boundaries (Ref 4, 15). Therefore, this study aims to characterize the effect of different post-printing heat treatments, i.e., annealing and quenching and tempering, on the corrosion performance of a WAAM fabricated 420 MSS with respect to the micro-constituents' evolution and texture annihilation during heat treatment.

2. Experimental Procedure

WAAM technology was adopted to fabricate a wall of 420 MSS on a 30-mm-thick base plate of AISI 420 stainless steel using ER420 feedstock wire. The chemical composition of both ER420 wire and AISI 420 substrate is reported in Table 1. As shown in Fig. 1, a gas metal arc welding (GMAW) torch mounted on a robotic arm, along with an automated wire feeding system was employed to fabricate a 25-layer wall with the dimensions of 160 × 160 × 6 mm^3 using an all-x scanning strategy and the inter-layer temperature of 100 °C (attained by ~ 7 min of dwelling time between the deposition of two consecutive layers). The implemented WAAM process parameters are summarized in Table 2. To eliminate the process-induced microstructural inhomogeneities and unfavorable phases, the as-printed samples were exposed to annealing and Q&T heat treatments. For annealing, the as-printed sample was held at 850 °C for 120 min, followed by cooling to room temperature in the furnace. For Q&T, the as-printed sample was first austenitized for 30 min at 1150 °C and then quenched in the air to room temperature. After a detailed investigation on the effect of several tempering temperatures on the electrochemical response of the samples (to be reported by the authors in another study), 400 °C was selected as the optimum tempering temperature. The as-quenched sample was then subjected to a 4 h tempering cycle at 400 °C, followed by air cooling.

For microstructural characterizations, samples were cut, mounted, and prepared following standard grinding and polishing procedures for stainless steels, and then etched using Villella's reagent for 20 s. The microstructural characteristics of the samples were studied using an FEI MLA 650F scanning electron microscope (SEM) equipped with an energy-dispersive x-ray spectroscopy (EDS) detector. Electron backscatter diffraction (EBSD) analysis was also conducted using an HKL EBSD system at the step size of 0.5 µm. X-ray diffraction (XRD) analysis was also performed using a Cu-K_α source at 40 kV and 30 mA.

The electrochemical behavior of the samples was examined through open circuit potential (OCP) and potentiodynamic polarization (PDP) testing. The electrochemical impedance spectroscopy (EIS) testing was also conducted to measure and analyse the electronic properties of the passive film formed on all samples. Electrochemical measurements were performed in aerated 3.5 wt.% NaCl solution using an IVIUM CompactStat™ computer controlled Potentiostat apparatus. A conventional three-electrode cell set-up, containing a saturated Ag/AgCl electrode as the reference electrode, a graphite rod as the counter electrode, and the prepared samples as the working

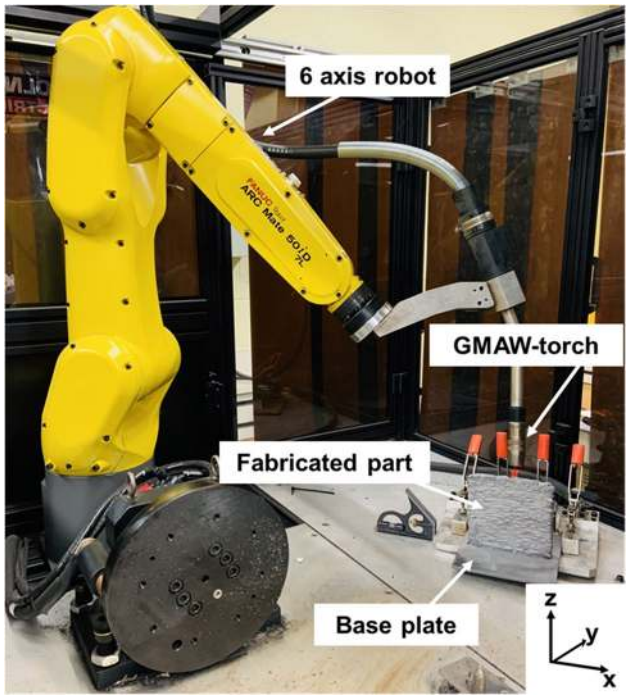

Fig. 1 The WAAM platform used for the fabrication of 420 MSS walls in this study

Table 1 The nominal chemical composition of the used materials in this study (all data in wt.%)

Material	C	Cr	Mn	Si	S	P	Ni	Mo	Cu	V	Fe
ER420	0.3–0.4	12–14	0–1	0–1	0–0.03	0–0.04	0–0.5	0–0.5	0–0.5	…	Bal.
AISI420	0.15–0.46	12–14	0.4–1	0–1	0–0.03	0–0.04	…	0–0.1	…	0.3	Bal.

Table 2 The WAAM process parameters used for the fabrication of AISI 420 MSS wall in this study

Current	Arc voltage	Wire feeding rate	Scanning rate	Ar flow rate
135 A	29 V	67.7 mm s^{-1}	3.6 mm s^{-1}	20 L min^{-1}

electrode were used. Prior to each PD and EIS experiments, the OCP values were also monitored for 1 h for stabilization. Separately, the OCP measurements were conducted over 14 h to analyse the electrochemical stability of samples over a longer period of time. The PDP tests were conducted at the scanning rate of 0.4 mV s^{-1} in the potential range of − 0.2 up to 0.5 V versus OCP. The EIS measurements were conducted over the frequency range of 10^5 to 10^{-2} Hz with a sinusoidal perturbation signal voltage of 10 mV after 1 and 120 h of immersion time. All electrochemical experiments for each condition were repeated at least five times to ensure reproducibility of the results.

3. Results

3.1 Microstructural Characterization

The low and high magnification SEM images of the as-printed sample and its corresponding EDS elemental maps of iron and chromium are illustrated in Fig. 2(a), (b), and (c). The low magnification micrograph of the as-printed sample (Fig. 2a) exhibits a columnar dendritic structure, grown along the building direction (*Z*-axis) parallel to the heat dissipation direction. As shown in Fig. 2(b), a fine lath martensitic structure (M phase) along with a high-volume fraction (∼20%) of δ-ferrite (DF) phase is formed in the as-printed part. While the formation of a martensitic structure containing δ-ferrite phase is not expected according to the pseudo-binary phase diagram of 420 MSS alloy (Ref 3), a martensitic matrix in the as-printed sample has formed due to the non-equilibrium solidification condition with relatively high cooling rate associated with the WAAM process (Ref 6). Moreover, the stabilization of the δ-ferrite phase at ambient temperature is correlated to the high chromium content of the alloy (Fig. 2c), as a ferrite stabilizing element, accompanied by the rapid solidification nature of process that hinders the diffusion-controlled transformation of δ-ferrite to austenite at ∼1400 °C (Ref 6). On the other hand, the Cr-EDX line scan analysis along the delta ferrite-matrix interface (Fig. 2c) revealed that in the area adjacent to the delta ferrite-matrix interface, Cr concentration reduced to less than 11 wt.%, confirming formation of Cr-depleted region at the interface in the as-printed sample.

Figure 2(d), (e), and (f) exhibits the SEM micrographs of the annealed sample and the corresponding EDS elemental maps of iron, chromium, and carbon elements. The annealed sample (Fig. 2d and e) revealed the suggested microstructure by the pseudo-binary phase diagram of 420 MSS alloy with islands of spherical chromium carbides embedded in a ferritic matrix (Ref 3). The EDS elemental map of the annealed sample (Fig. 2f) shows enrichment in chromium and carbon and depletion in iron, indicating the formation of chromium-rich carbides.

SEM micrographs of the Q&T sample at three different magnifications are shown in Fig. 2(g), (h), and (i). The formation of a fully martensitic matrix without any undissolved carbides (coarse spherical carbides) and dissolution of δ-ferrite phase were detected in the as-quenched sample before tempering, indicating the samples' proper austenitization at 1150 °C. Austenite grains are formed through austenitization and transformed on cooling, while the segregation of chromium carbides at the prior austenite grain boundaries (PAGBs) (see Fig. 2h) and the formation of sub-micron intra-lath chromium carbides occurred during the tempering process (Fig. 2i). Previous studies on the MSS with 13 wt.% chromium content (Ref 16, 17) suggested that the intra-lath carbides formed at low tempering temperatures (∼400 °C) were mainly characterized as nano-sized M_3C type carbides with similar Cr-concentration to the martensitic matrix.

The XRD patterns of the as-printed, annealed, and the Q&T samples are shown in Fig. 3. The XRD spectra of the as-printed sample exhibit the presence of martensitic phase at (110), (200), (211), and (220) planes along with low-intensity peaks of austenite phase (γ) at (111) and (200) planes. Presence of $(111)_\gamma$ and $(200)_\gamma$ peaks indicates the formation of retained austenite phase through the solidification process due to the sequential heating and cooling cycles associated with the WAAM process and also the noticeable content of carbon as an austenite stabilizing element in the alloy (Ref 6, 14). The formation mechanism of the retained and reversed austenite in the WAAM-420 stainless steel is thoroughly explained in the authors' previous works (Ref 13, 14). No δ-ferrite peaks were distinguished on the XRD spectra due to only minor variation of lattice parameters between martensite and δ-ferrite phases (10^{-4}–10^{-5} nm) (Ref 18). The XRD spectra of the annealed and Q&T samples show the same ferritic/martensitic peaks as the as-printed sample, while the $(111)_\gamma$ and $(200)_\gamma$ are disappeared after annealing and tempering cycles. During the Q&T heat treatment process, the sample experiences a single fast cooling cycle from the austenitizing temperature, and the tempering temperature (400 °C) is not sufficient to activate the reversed austenite formation. On the other hand, during the annealing process, the diffusional segregation of carbon element from the austenite phase to the ferritic matrix eliminates the retained austenite phase from the as-printed structure.

3.2 Crystallographic Orientation Characterization

Figure 4(a), (b), and (c) illustrates the inverse pole figure (IPF) maps superimposed on the grain boundaries maps for the as-printed, annealed, and the Q&T samples, respectively. The IPF of the as-printed sample reveals a fine martensitic lath structure formed within the coarse primary austenite grains (marked with black lines) with several crystallographic orientations normal to {001}, {101}, and {111} planes. Unlike the as-printed sample, the IPF map of the annealed sample (Fig. 4b) reveals an equiaxed and coarser grain structure. Moreover, as shown in Fig. 4(c), the IPF of the Q&T sample exhibits a tempered martensitic structure, characterized by a three-level

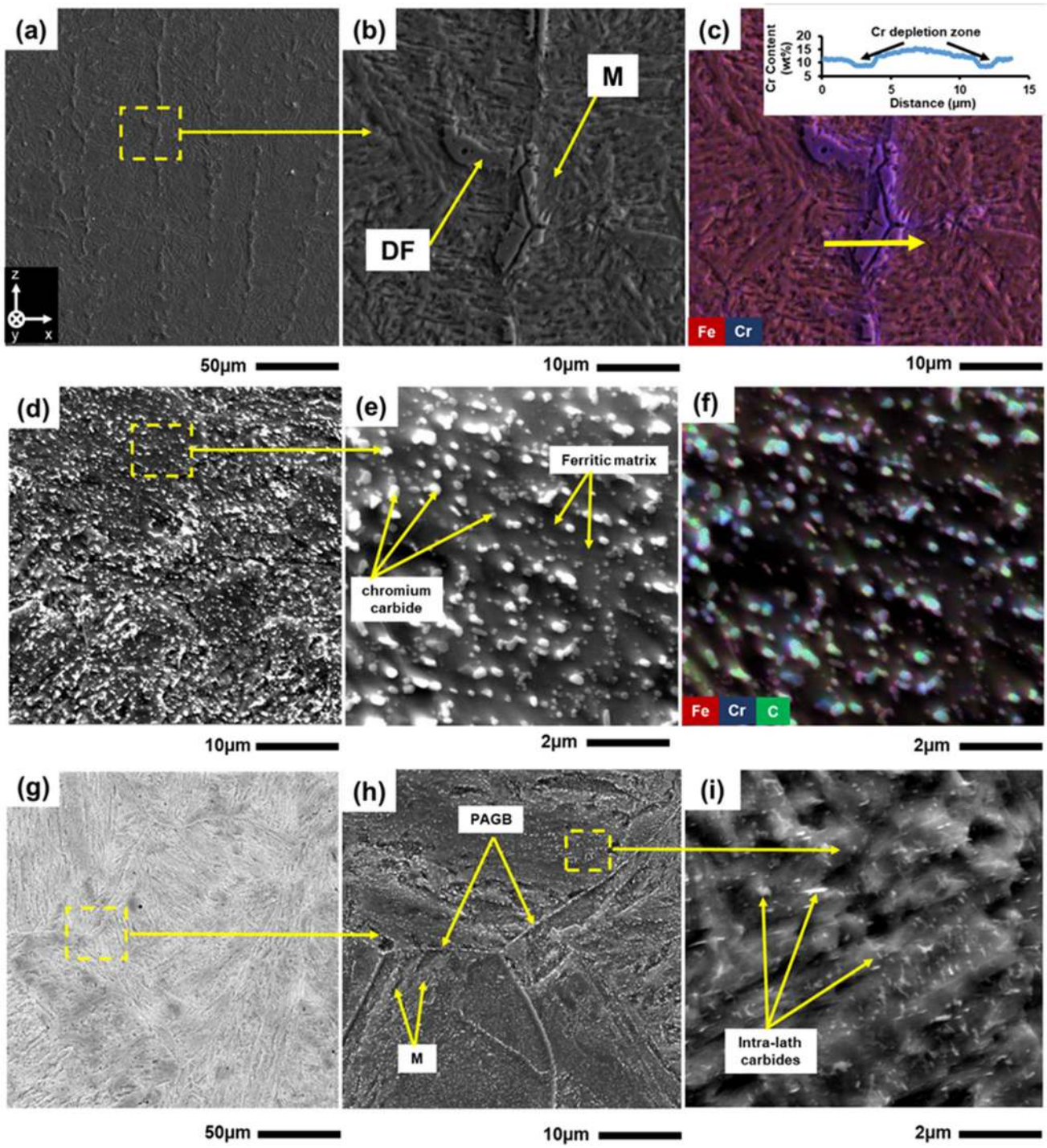

Fig. 2 (a) Low magnification SEM micrograph of the as-printed sample along with (b) its high magnification SEM showing the formation of the δ-ferrite phase and (c) its corresponding EDS elemental map and line scan showing high concentration of Cr in the δ-ferrite phase, (d and e) multi-scale SEM micrographs of the annealed sample showing islands of spherical carbides in a ferritic matrix and (f) its corresponding EDS elemental map showing high concentration of Cr and C in the spherical carbides, (g) low magnification SEM micrograph of the Q&T and (f) high magnification SEM showing PAGBs, intergranular carbides, and martensitic phase, and (i) formation of intra-lath carbides in the martensitic phase

hierarchy within its morphology, i.e., martensite lath, block, and packet, confined within the PAGBs (marked with black lines). Distribution of low angle grain boundaries (LAGBs), medium angle grain boundaries (MAGBs), and high angle grain boundaries (HAGBs) for the as-printed, annealed, and Q&T samples are exhibited in Fig. 4(d), (e), and (f). It is notable that the distributions of the LAGBs and HAGBs remain relatively the same for the as-printed and the Q&T samples, while the annealed sample exhibits a significantly lower fraction of LAGBs and a higher fraction of HAGBs. Statistical illustration of the misorientation angle distribution at Fig. 4(j) reveals that the fraction of the LAGBs for the annealed sample

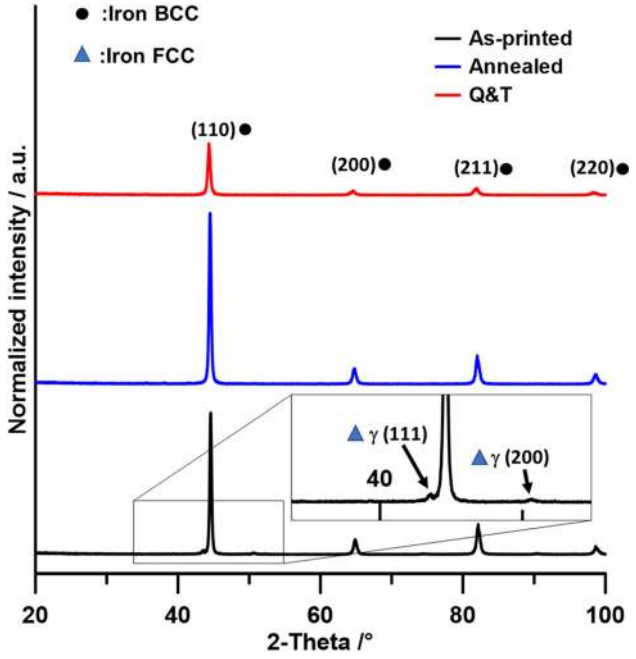

Fig. 3 The XRD results of the as-printed, annealed, and Q&T samples

is ~11%, while this fraction is ~51 and ~56% for the as-printed and Q&T samples, respectively. Additionally, Fig. 4(g), (h), and (i) illustrates the grain and lath size distributions, extracted from the EBSD data, representing the size of martensite laths for the as-printed and Q&T samples and the ferrite grain size for the annealed sample. Both as-printed and Q&T samples exhibit a high fraction of relatively fine lath structure (average lath size ~ 2.50 µm), while the annealed sample exhibits relatively coarser grain structure with an average grain size of ~ 5.25 µm.

The pole figures (PFs) of the as-printed, annealed, and Q&T samples at {100}, {110}, and {111} planes are demonstrated in Fig. 5, and the building direction (BD) and the deposition direction (DD) are marked as well. The PF of the as-printed sample (Fig. 5a) exhibits a strong cubic texture at {100} planes (maximum intensity of ~4.22 MUD), ascribed to the directional solidification along the maximum thermal gradient direction (Ref 7). Contrarily, the pole figures of annealed and Q&T samples (Fig. 5b and c) exhibit relatively weaker texture, ascribed to the elimination of solidification texture during recrystallization (in the annealed sample) or austenitization (for the Q&T sample). The orientation distribution function (ODF) maps based on the PF stereographs at φ_2=45° associated with the detailed crystallographic orientation of each texture component and their corresponding 3D plots are shown in Fig. 6. Figure 6(a) and (b) exhibits a strong dominancy of preferred columnar {001}<100> solidification texture combined with {111}<110> texture component with the maximum intensity of 6.52, while significantly weaker columnar {001}<100> texture is observed for the heat-treated samples (Fig. 6c, d, e, and f). The annealed sample exhibits {111}<110> and {011}<111> texture components along with full elimination of {001}<100> solidification texture (Fig. 6c), ascribed to occurrence of severe recrystallization during annealing, while weak {001}<100> and {011} <111> texture components are observed for the Q&T sample (Fig. 6e).

3.3 Corrosion Results

The OCP values variations over 14 h in aerated 3.5 wt.% NaCl solution for the as-printed and heat-treated samples are displayed in Fig. 7(a). The OCP trend relatively stabilized after nearly 9.7 h, and the average stabilized OCP value for the as-printed sample was found to be -390 ± 20 $mV_{Ag/AgCl}$, while it increases to -365 ± 15 $mV_{Ag/AgCl}$ and -315 ± 25 $mV_{Ag/AgCl}$ for the annealed and Q&T samples, respectively. Severe fluctuations were observed in the OCP values of the annealed and Q&T samples at the initial monitoring times (immersion time $\leq 10^4$ s), possibly ascribed to continuous metastable pitting or some type of localized attack on the samples surfaces (Ref 3) that eventually decreases the OCP value at immersion times higher than 10^4 s.

Following the OCP measurements, the PDP experiments were conducted to characterize the electrochemical behavior of the samples, as shown in Fig. 7(b). The obtained electrochemical parameters from the PDP graphs, i.e. corrosion current density (i_{corr}), corrosion potential (E_{corr}), pitting potential (E_{pit}), and passivation current density (i_p) are summarized in Table 3. A wide passive region with clear breakdown potential was observed for the Q&T sample, while an active-like behavior, characterized by a rapid increase of the anodic current density at potentials higher than E_{corr}, was detected for the as-printed and annealed samples, suggesting the continuous occurrence of severe localized corrosion attacks that hinder the formation of an intact passive film on the samples' surfaces. The observed fluctuations in the anodic branch for the Q&T sample also correspond to metastable pitting (Ref 3). The Q&T sample exhibited higher E_{corr} and lower i_{corr} values as compared to the as-printed and annealed samples, indicating its lower corrosion susceptibility and higher electrochemical stability, consistent with the OCP trends.

In order to analyse the protectiveness and stability of the passive film on the samples' surfaces, the EIS experiments were conducted in aerated 3.5 wt.% NaCl electrolyte. Figure 8 shows the obtained Nyquist diagrams for the as-printed and heat-treated samples, after 1 and 120 h of immersion times. Nyquist diagrams of all samples exhibited one broad capacitive semicircle, as a result of the superposition of two individual peaks with neutral time constants for both immersion times (Ref 15). The significantly larger semicircle curves in the Nyquist diagrams for the Q&T sample at both immersion times as compared to the other two samples confirm the more protective nature of the passive film formed on the Q&T sample (Ref 15), consistent with the observed trend in the PDP results. After the longer immersion time of 120 h, a significant reduction in the radius of the Nyquist curves was detected, ascribed to the continuous dissolution of the passive layer into the solution over time, causing severe deterioration in the electrochemical stability (Ref 15). As shown in Fig. 8(a), a simplified equivalent circuit (SEC) was fitted to the EIS data to quantitatively analyse the passive film evolution on the samples' surfaces. The obtained fitted results are also plotted on the Nyquist diagrams (Fig. 8a and b). In the used SEC model, R_s corresponds to the electrolyte resistance, CPE_p and R_p represent the capacitance and the resistance of the passive film, CPE_{dl} and R_{ct} correspond to the double layer constant phase element (CPE) and its charge transfer resistance, respectively (Ref 4). The impedance value of the CPE can be described as: $Z_{CPE} = [Y_0(j\omega)^n]^{-1}$, where Y_0 is the CPE constant, ω is the angular frequency, n is the dispersion

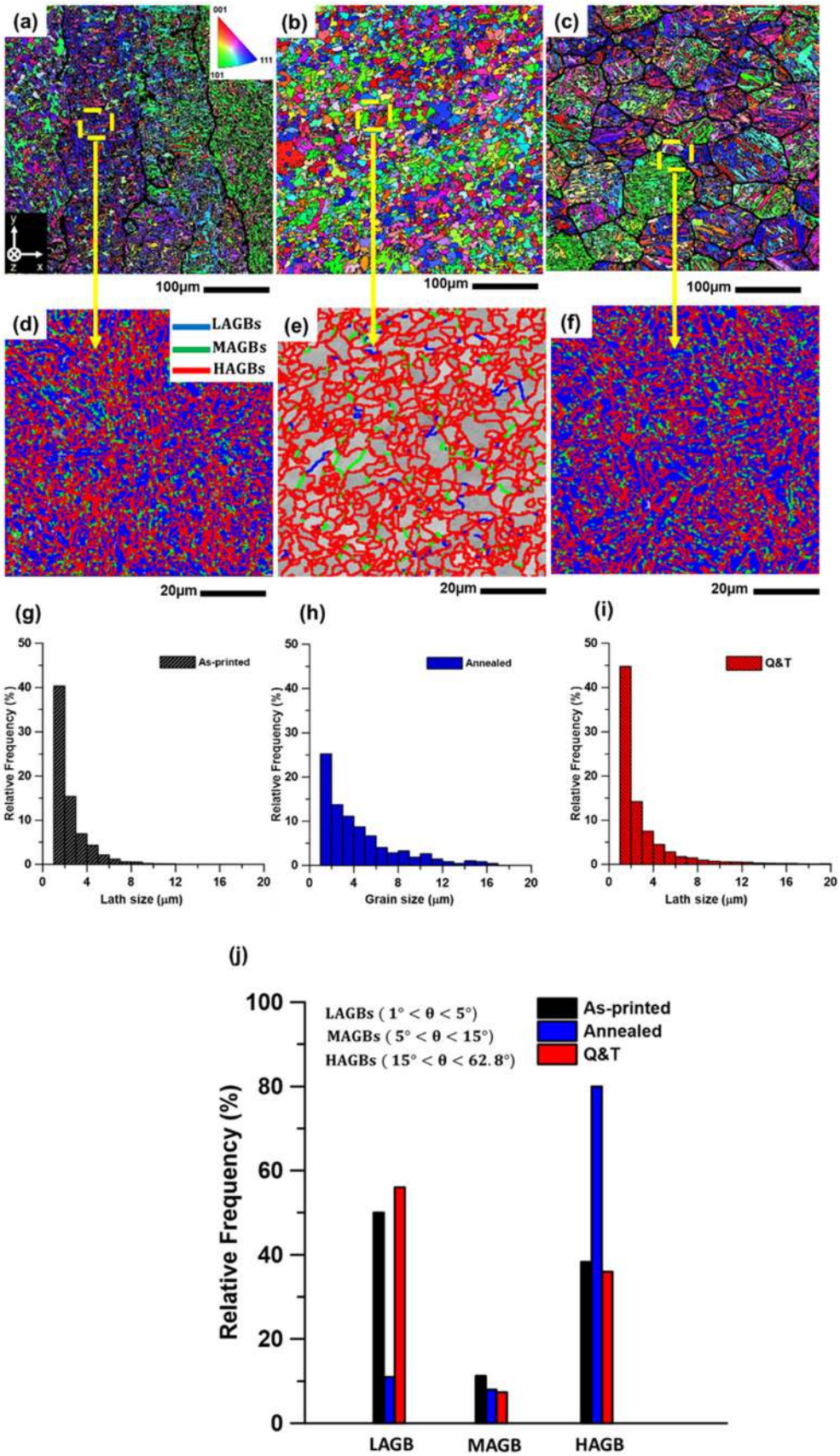

Fig. 4 (a-c) The IPF maps superimposed on the grain boundary maps for the as-printed, annealed, and the Q&T samples, respectively, (d-f) the corresponding grain boundaries misorientation maps, (g-i) grain size distribution plots, and (j) grain boundaries misorientation angles distributions for the studied samples

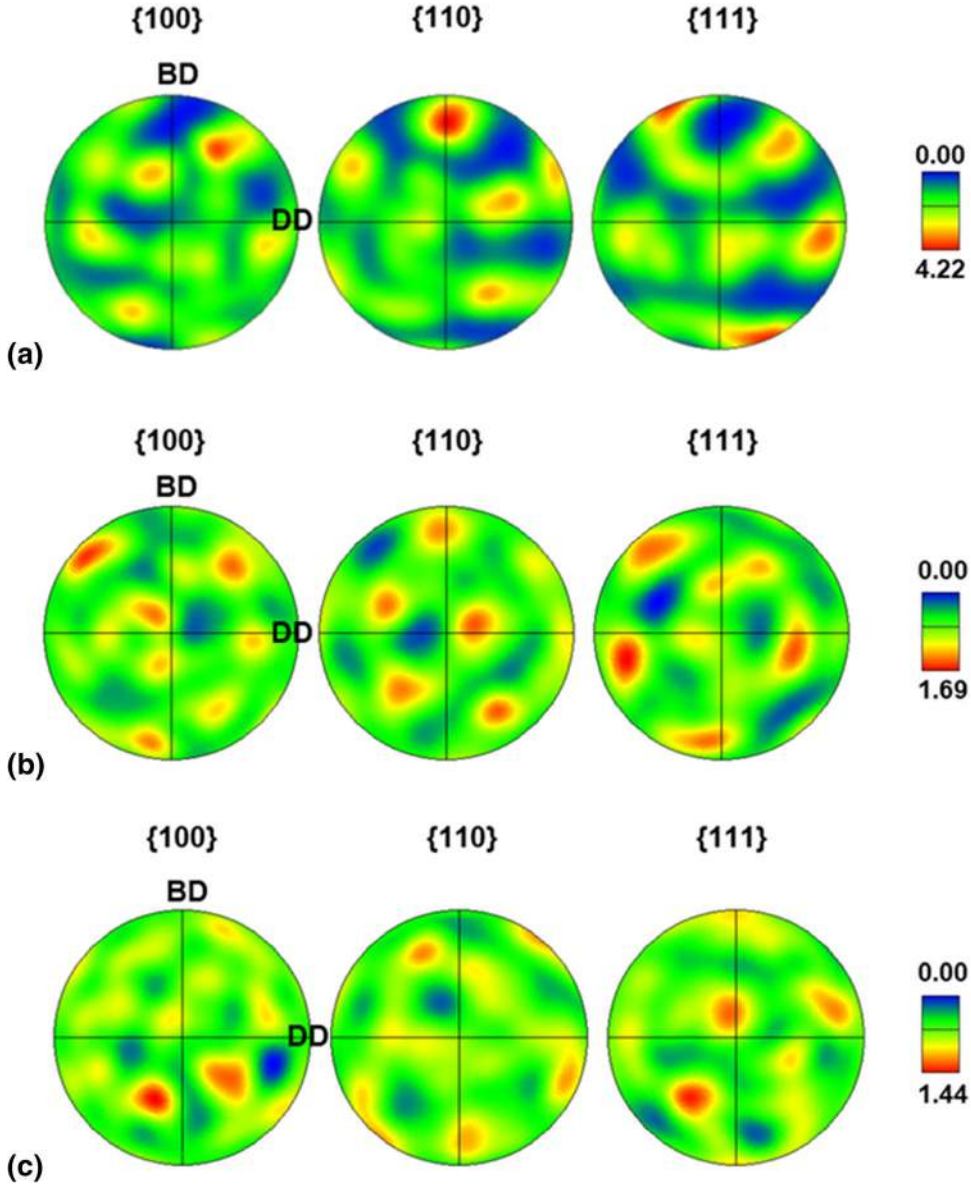

Fig. 5 EBSD pole figure maps of (a) the as-printed, (b) annealed, and (c) the Q&T samples

coefficient of the CPE, and $j = -(1)^{1/2}$ (Ref 4). The fitting parameters obtained from the EIS results are summarized in Table 4. At both immersion times of 1 and 120 h, the Q&T sample showed higher R_{ct} and lower CPE_{dl} values as compared to the other two samples, revealing the more protective nature of the passive layer against localized attack on the Q&T sample. Significantly lower R_{ct} and R_p values at 120 h as compared to the samples immersed for 1 h indicate the reduced stability of the passive film at longer immersion times in the electrolyte. The obtained lower R_{ct} values than their corresponding R_p values for the as-printed and annealed samples at both immersion times confirms the active-like behavior of the samples' surfaces, while an opposite trend ($R_p < R_{ct}$) was detected for the Q&T sample, indicating its clear passive behavior.

The power-law model developed by Hirschorn et al. (Ref 19), is used as a practical technique to analyse the CPE parameters in terms of passive film thickness and resistance. In this model (Ref 19), the C_{eff} is described as: $C_{eff} = gQ(\rho_\delta \varepsilon_0 \varepsilon)^{1-n}$, where ε is the passive film dielectric constant ($\sim$15.6 for Cr_2O_3), ε_0 is the vacuum permittivity (8.854×10^{-14} F cm^{-1}) (Ref 20), g is a function of n ($g = 1 + 2.88(1-n)^{2.375}$), and ρ_δ is the passive layer resistance at its maximum thickness. The passive layer thickness in steady-state condition (L_{ss}) can be estimated based on the EIS data and using the plate capacitor relationship as suggested in (Ref 15, 21): $L_{ss} = \frac{\varepsilon \varepsilon_0 A}{C_{eff}}$, where A is the is the surface area of the corroded sample. The calculated L_{ss} and C_{eff} values for the samples, presented in Table 5, confirmed a higher passive layer thickness for the Q&T sample, while it decreases for the other

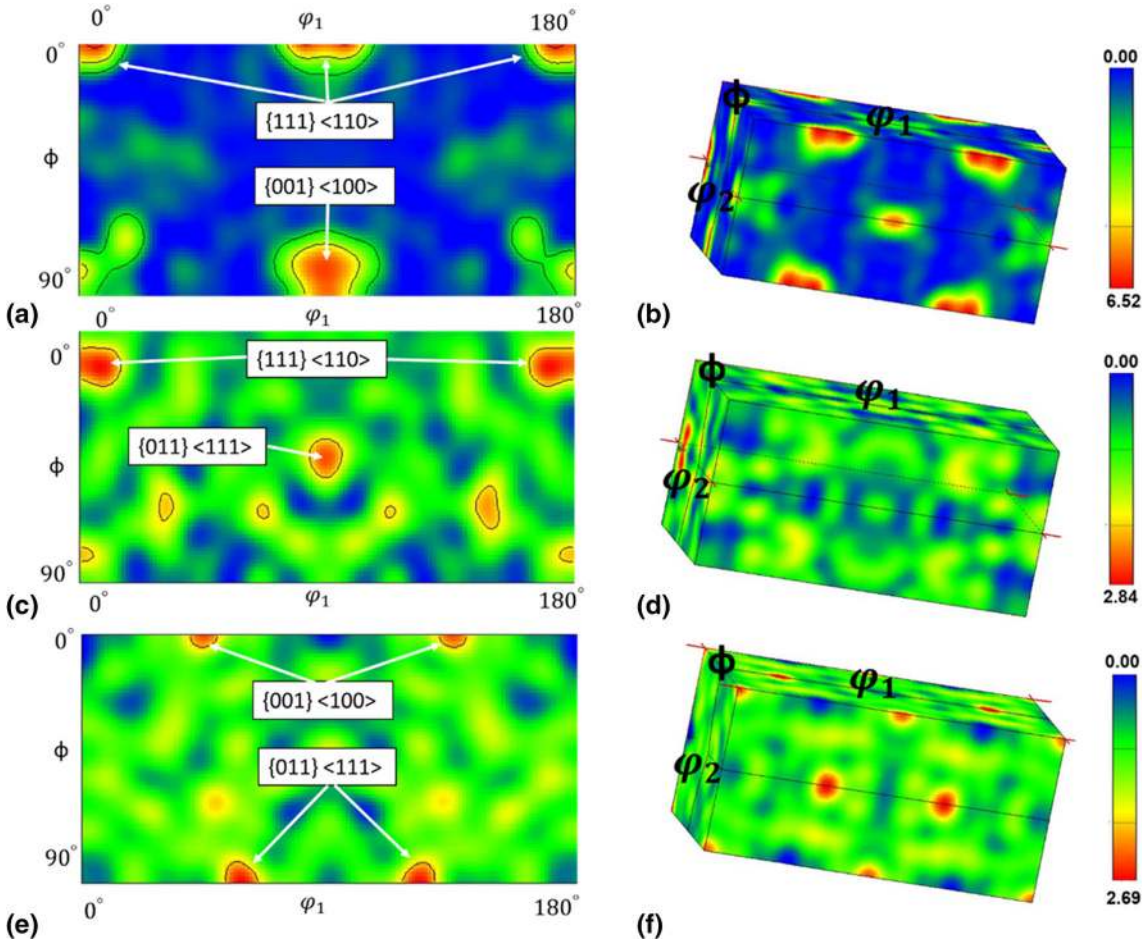

Fig. 6 Angular textural cross-sections of orientation distribution function at φ_2=45° and their corresponding 3D-plots for (a and b) the as-printed, (c and d) annealed, and (e and f) the Q&T samples

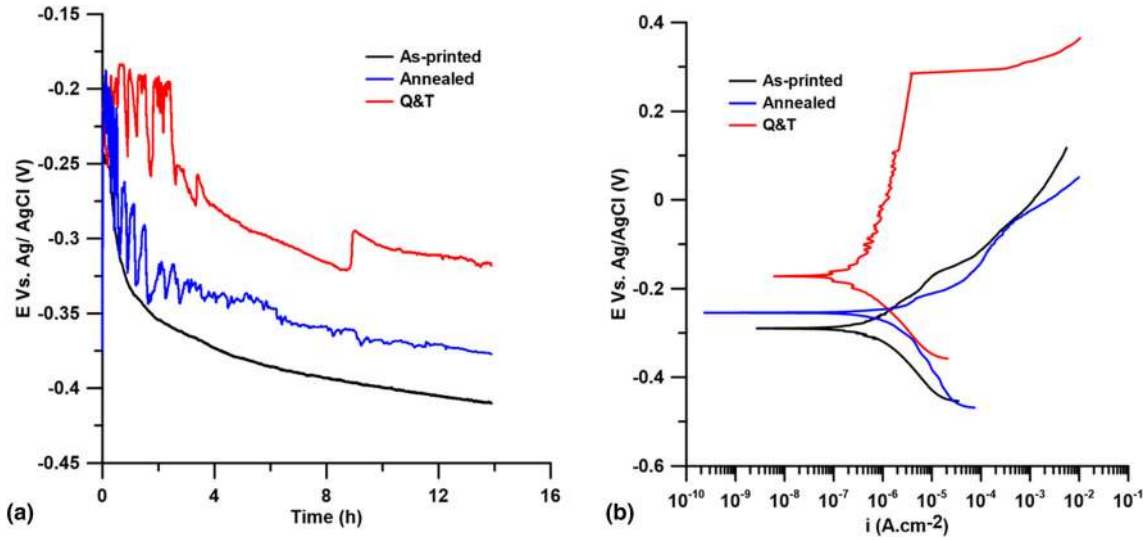

Fig. 7 (a) The open circuit potential (OCP) values versus time, (b) potentiodynamic polarization curves for the as-printed, annealed, and the Q&T samples in aerated 3.5 wt.% NaCl solution

Table 3 The electrochemical parameters extracted from the PDP graphs in aerated 3.5 wt.% NaCl solution at room temperature

Sample	E_{corr}, $mV_{Ag/AgCl}$	i_{corr}, μA cm^{-2}	i_p, μA cm^{-2}	E_{pit}, $mV_{Ag/AgCl}$
As-printed	− 293±12	0.62±0.05	…	…
Annealed	− 258±15	0.44±0.03	…	…
Q&T	− 176±13	0.21±0.04	8.256±0.04	302±15

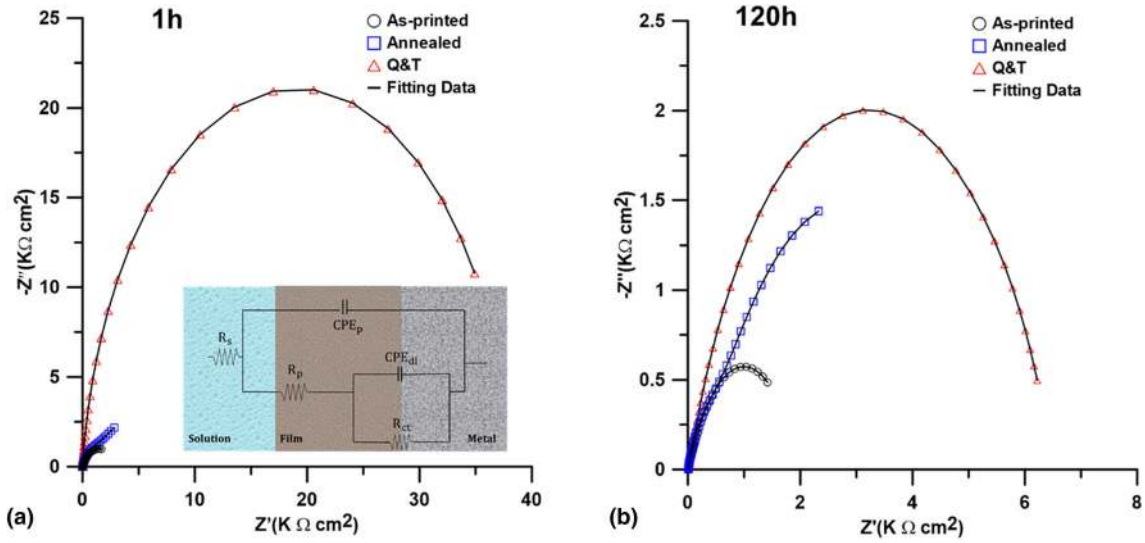

Fig. 8 Nyquist plots and the corresponding equivalent circuit model used to describe the EIS data at immersion times of (a)1 h, (b) 120 h

Table 4 The fitted electrochemical parameters for the EIS spectra

Immersion time, h	Sample	R_s, Ω cm^2	CPE_p, Ω^{-1} $cm^{-2}s^n$	n_1	R_p, Ω cm^2	CPE_{dl}, Ω^{-1} $cm^{-2}s^n$	n_2	R_{ct}, Ω cm^2	$\sum\chi^2$
1	As-printed	3.54	1.75×10^{-4}	0.89	1.40×10^{4}	1.33×10^{-4}	0.88	1.89×10^{2}	1.27×10^{-5}
	annealed	3.56	6.82×10^{-5}	0.96	2.60×10^{4}	5.74×10^{-5}	0.94	1.93×10^{3}	1.64×10^{-5}
	Q&T	3.58	9.27×10^{-6}	0.94	1.19×10^{2}	2.62×10^{-5}	0.86	1.90×10^{5}	1.62×10^{-5}
120	As-printed	3.54	9.94×10^{-4}	0.89	6.04×10^{3}	1.83×10^{-4}	0.83	1.03×10^{2}	1.52×10^{-5}
	annealed	3.58	4.23×10^{-4}	0.88	1.74×10^{3}	1.25×10^{-3}	0.84	1.24×10^{3}	1.47×10^{-5}
	Q&T	3.65	8.24×10^{-5}	0.87	1.12×10^{2}	2.71×10^{-2}	0.98	7.5×10^{3}	1.25×10^{-5}

Table 5 The calculated capacitance (C_{eff}) and passive layer thickness (L_{ss})

Immersion time, h	Sample	C_{eff}, F cm^{-2}	L_{ss}, nm
1	As-printed	6.52×10^{-4}	0.52
	annealed	4.06×10^{-4}	1.07
	Q&T	1.45×10^{-5}	61.23
120	As-printed	8.24×10^{-4}	0.25
	annealed	6.03×10^{-4}	0.43
	Q&T	4.62×10^{-5}	18.05

samples in the order of annealed sample > as-printed sample, consistent with the OCP, PDP, and EIS results.

4. Discussion

It is well-known that the electrochemical response of MSSs is highly dependant on the formation of micro-constituents, where micro-galvanic coupling between the anodic martensitic/ferritic matrix and cathodic carbides (mostly chromium

carbides) governs the localized corrosion attack (Ref 3). The same scenario can be seen in the WAAM 420 MSS, where δ-ferrite phase possessing a high content of chromium, plays the same role as cathodic intergranular carbides, and can adversely impact the corrosion performance (Ref 14). Regions at the periphery of the δ-ferrite phase are mostly chromium depleted (shown in Fig. 2c), since the Cr-rich δ-ferrite phase drains the chromium element from its adjacent matrix, causing the susceptibility of the δ-ferrite/martensite interface to initiation of corrosion attack (Ref 14). Such corrosion attack initiation sites were observed at the interface of the δ-ferrite phase and martensitic matrix in the as-printed sample, after the PDP test, as shown in Fig. 9(a) and (b). The EDS elemental maps (Fig. 9c and d) revealed the sensitized regions with high concentration of chromium at the δ-ferrite/matrix interface due to the preferential dissolution of Fe element (Fig. 9c) during the corrosion testing, while Cr element does not seem to leach from the surface (Ref 4, 15). The presence of a high fraction of δ-ferrite phase ($\sim$ 20%) in the microstructure of the as-printed sample provokes the occurrence of micro-galvanic coupling between the cathodic delta ferrite phase and the Cr-depleted martensitic matrix and acts as the main factor for deterioration of the electrochemical response and active-like behavior of this sample (Ref 13). Similarly, the active behavior of the annealed sample through the PDP test is ascribed to the high-volume fraction of intergranular chromium carbides at the ferritic matrix and higher susceptibility of matrix/carbide interface to the pitting initiation (Ref 4, 5). The corrosion morphology of the annealed sample (Fig. 9e and f) revealed stable pit growth on its surface, characterized by the formation of propagated pitting sites resulted from continuous growth and coalescence of the pits as the corrosion progresses. The EDS mapping from one of the surface pits revealed selective dissolution of Fe element from the pit and its border, creating a Cr-rich band

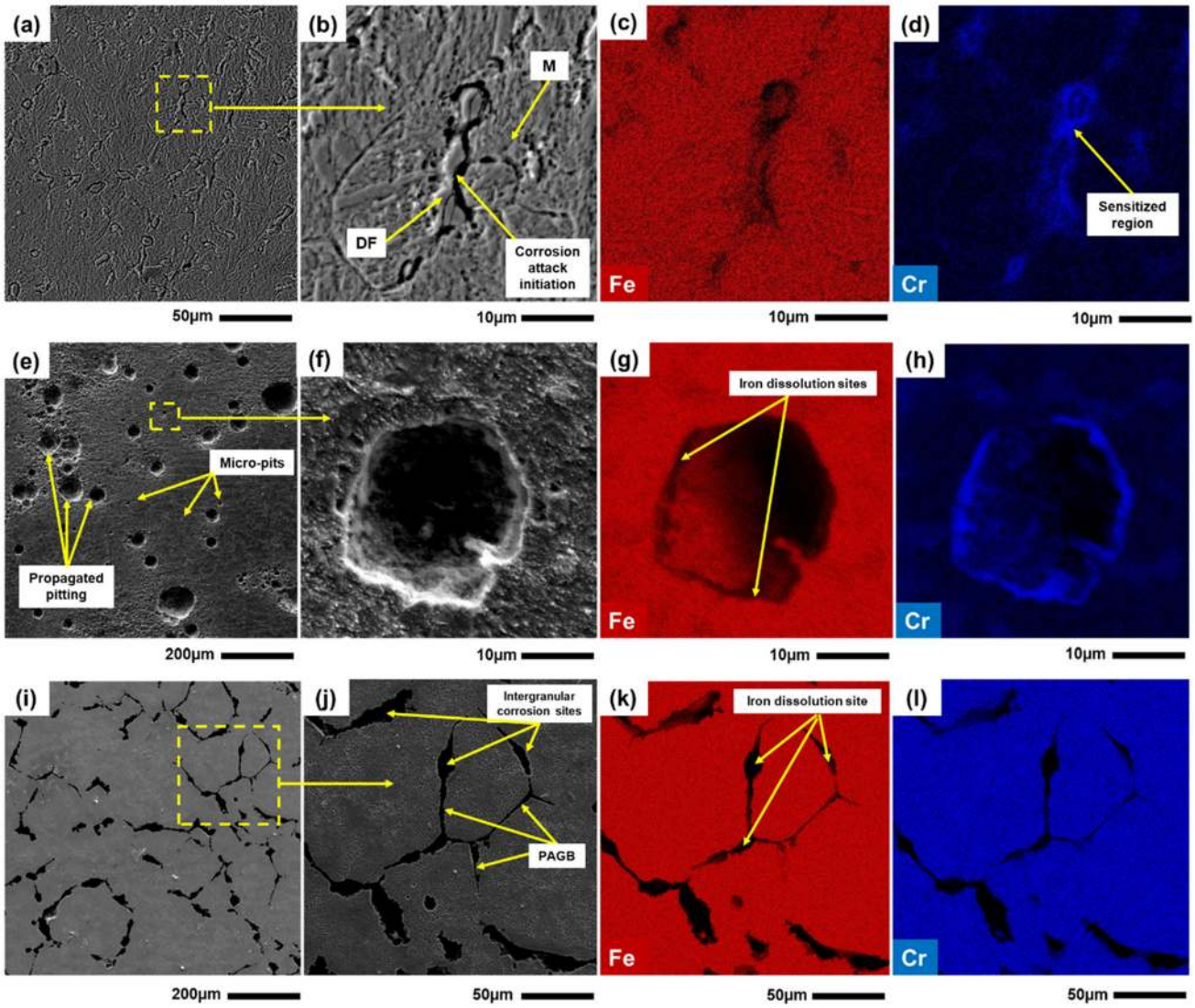

Fig. 9 (a) The SEM micrographs from the as-printed sample after polarization testing, (b) higher magnification SEM micrograph from the enclosed area in (a), (c and d) the corresponding EDX-Fe and EDX-Cr concentration maps, respectively, (e) the SEM micrographs from the annealed sample after polarization testing, (f) higher magnification SEM micrograph from the enclosed area in (f) showing the micro-pit formation, (g and h) the corresponding EDX-Fe and EDX-Cr concentration maps, respectively, (i) the SEM micrographs from the Q&T sample after polarization testing, (j) higher magnification SEM micrograph from the enclosed area in (i), and (k and l) the corresponding EDX-Fe and EDX-Cr concentration maps, respectively

along its periphery (Fig. 9g and h). As shown in Fig. 9(i), (j), (k), and (l), the corrosion mechanism of the Q&T sample is controlled by the intergranular corrosion at the PAGBs, where a chromium depleted region is formed through precipitation of the intergranular carbides adjacent to the high energy grain boundaries. Interestingly, it is observed that the martensitic matrix in the interior of PAGs is highly resistant to localized corrosion, possibly attributed to the chemical composition of the intra-lath carbides (see Fig. 2i) (Ref 16, 17). Previous studies have revealed that the morphology, size, and chemical composition of tempered carbides are highly dependent on the tempering temperature (Ref 16, 17). The intra-lath carbides formed at 400 °C are mostly nano-sized M_3C type carbides with chemical composition and chromium concentration similar to the martensitic matrix (Ref 16, 17), hindering the micro-galvanic coupling effect at their interface with the matrix, leading to the formation of a uniform passive layer on the Q&T sample.

In addition to the impact of secondary phases as the dictating factor that controls the corrosion behavior of the studied alloy, the distribution of grain boundary misorientation maps for the as-printed and heat-treated samples herein (Fig. 4j) revealed that the annealed sample possesses a significantly lower fraction of LAGBs and higher fraction of HAGBs, while the fractions of LAGBs and HAGBs are relatively constant for the as-printed and the Q&T sample. According to the Read-Shockley equation (Ref 22), the amount of stored energy in the grain boundaries is proportional to the grain boundaries misorientation angle with some exceptions, such as twin boundaries. Although not significant, this can be considered as a minor contributing factor to the reduced corrosion performance of the annealed sample with a high fraction of high energy HAGBs, where fast diffusion paths can be easily activated (Ref 23). The noticeable higher fraction of LAGBs in the Q&T sample can support the formation of a more uniform passive film on its surface resulted from proximity of the grain boundary diffusivity and the material's bulk diffusivity (Ref 23).

5. Conclusions

In this study, the effects of different heat treatment processes, i.e., annealing and quenching and tempering (Q&T) cycles, on the electrochemical stability of a WAAM fabricated 420 MSS were investigated. The microstructure of the as-printed sample contained martensite laths with an average lath size of ~ 2.5 µm along with the delta ferrite phase. The annealed sample exhibited islands of spherical chromium carbides embedded in a ferritic matrix, while the Q&T sample showed intergranular carbides precipitated at the PAGBs, and sub-micron intra-lath carbides. While the as-printed sample exhibited strong $\{001\}<100>$ solidification texture, the annealed and Q&T samples showed relatively weaker texture components, ascribed to the elimination of solidification texture during phase transformations. The PDP and EIS testing revealed the formation of a uniform passive film on the Q&T sample, while an active-like behavior was observed for the as-printed and annealed samples. The higher corrosion potential and lower corrosion current density of the Q&T sample consistent with its Nyquist's larger capacitive loop confirmed its better electrochemical response as compared to the other two samples. The corrosion morphology of the samples after the PDP test revealed severe localized corrosion attack on the as-printed sample, severe localized pitting on the annealed sample, and early stage of intergranular corrosion at the PAGBs on the Q&T sample. The superior corrosion response of the Q&T sample was attributed to the formation of intra-lath M_3C type carbides with similar chemical composition to the matrix and lack of sensitized regions on its surface.

Acknowledgments

The authors would like to thank the support of Suncor Energy, Memorial University of Newfoundland, Dalhousie University, Canada Research Chair (CRC) program, and Mitacs organization for sponsoring this work.

References

1. M.K. Alam, M. Mehdi, R.J. Urbanic, and A. Edrisy, Mechanical Behavior of Additive Manufactured AISI 420 Martensitic Stainless Steel, *Mater. Sci. Eng. A*, 2020, **773**, p 138815
2. A.N. Isfahany, H. Saghafian, and G. Borhani, The Effect of Heat Treatment on Mechanical Properties and Corrosion Behavior of AISI420 Martensitic Stainless Steel, *J. Alloys Compd.*, 2011, **509**(9), p 3931–3936
3. K.H. Anantha, C. Ornek, S. Ejnermark, A. Medvedeva, and J. Sj, Correlative Microstructure Analysis and In Situ Corrosion Study of AISI 420 Martensitic Stainless Steel for Plastic Molding, *J. Electrochem. Soc.*, 2017, **164**(4), p 85–93
4. S. Salahi, M. Kazemipour, and A. Nasiri, Effect of Uniaxial Tension-Induced Plastic Strain on the Microstructure and Corrosion Behavior of 13Cr Martensitic Stainless Steel, *Corrosion*, 2020, **76**, p 1122–1135
5. S. Salahi, M. Kazemipour, and A. Nasiri, Effects of Microstructural Evolution on the Corrosion Properties of AISI 420 Martensitic Stainless Steel during Cold Rolling Process, *Mater. Chem. Phys.*, 2021, **258**, p 123916
6. M. Ghaffari, A.V. Nemani, and A. Nasiri, Interfacial Bonding between a Wire Arc Additive Manufactured 420 Martensitic Stainless Steel Part and Its Wrought Base Plate, *Mater. Chem. Phys.*, 2020, **251**, p 123199
7. F. Khodabakhshi, M.H. Farshidianfar, A.P. Gerlich, M. Nosko, V. Trembošová, and A. Khajepour, Effects of Laser Additive Manufacturing on Microstructure and Crystallographic Texture of Austenitic and Martensitic Stainless Steels, *Addit. Manuf.*, 2020, **31**, p 100915
8. H. Chae, E.-W. Huang, W. Woo, S.H. Kang, J. Jain, K. An, and S.Y. Lee, Unravelling Thermal History during Additive Manufacturing of Martensitic Stainless Steel, *J. Alloys Compd.*, 2020, **857**, p 157555
9. M. Rafieazad, M. Ghaffari, A.V. Nemani, and A. Nasiri, Microstructural Evolution and Mechanical Properties of a Low-Carbon Low-Alloy Steel Produced by Wire Arc Additive Manufacturing, *Int. J. Adv. Manuf. Technol.*, 2019, **105**(5–6), p 2121–2134
10. A. Vahedi Nemani, M. Ghaffari, and A. Nasiri, On the Post-Printing Heat Treatment of a Wire Arc Additively Manufactured ER70S Part, *Materials (Basel)*, 2020, **13**(12), p 2795
11. A.V. Nemani, M. Ghaffari, S. Salahi, J. Lunde, and A. Nasiri, Effect of Interpass Temperature on the Formation of Retained Austenite in a Wire Arc Additive Manufactured ER420 Martensitic Stainless Steel, *Mater. Chem. Phys.*, 2021, **266**, p 124555
12. A.V. Nemani, M. Ghaffari, S. Salahi, and A. Nasiri, Effects of Post-Printing Heat Treatment on the Microstructure and Mechanical Properties of a Wire Arc Additive Manufactured 420 Martensitic Stainless Steel Part, *Mater. Sci. Eng. A*, 2021, **813**, p 141167
13. J. Lunde, M. Kazemipour, S. Salahi, and A. Nasiri, Microstructure and Mechanical Properties of AISI 420 Stainless Steel Produced by Wire Arc Additive Manufacturing, in *TMS 2020 149th Annual Meeting and Exhibition Supplemental Proceedings* (Springer, 2020), pp. 413–424
14. M. Kazemipour, J.H. Lunde, S. Salahi, and A. Nasiri, On the Microstructure and Corrosion Behavior of Wire Arc Additively Manufactured AISI 420 Stainless Steel, in *TMS 2020 149th Annual*

Meeting & Exhibition Supplemental Proceedings (Springer, 2020), pp. 435–448
15. S. Salahi, M. Kazemipour, and A. Nasiri, Effects of Microstructural Evolution on the Corrosion Properties of AISI 420 Martensitic Stainless Steel during Cold Rolling Process, *Mater. Chem. Phys.*, 2020, **258**, p 123916
16. S.K. Bonagani, V. Bathula, and V. Kain, Influence of Tempering Treatment on Microstructure and Pitting Corrosion of 13 wt.% Cr Martensitic Stainless Steel, *Corros. Sci.*, 2018, **131**, p 340–354
17. S.-Y. Lu, K.-F. Yao, Y.-B. Chen, M.-H. Wang, X. Liu, and X. Ge, The Effect of Tempering Temperature on the Microstructure and Electrochemical Properties of a 13 wt.% Cr-Type Martensitic Stainless Steel, *Electrochim. Acta*, 2015, **165**, p 45–55
18. J. Ge, J. Lin, Y. Chen, Y. Lei, and H. Fu, Characterization of Wire Arc Additive Manufacturing 2Cr13 Part: Process Stability, Microstructural Evolution, and Tensile Properties, *J. Alloys Compd.*, 2018, **748**, p 911–921
19. B. Hirschorn, M.E. Orazem, B. Tribollet, V. Vivier, I. Frateur, and M. Musiani, Constant-Phase-Element Behavior Caused by Resistivity Distributions in Films: I. Theory, *J. Electrochem. Soc.*, 2010, **157**(12), p 452
20. A. Fattah-Alhosseini, M.A. Golozar, A. Saatchi, and K. Raeissi, Effect of Solution Concentration on Semiconducting Properties of Passive Films Formed on Austenitic Stainless Steels, *Corros. Sci.*, 2010, **52**(1), p 205–209
21. M. Rafieazad, M. Mohammadi, A. Gerlich, and A. Nasiri, Enhancing the Corrosion Properties of Additively Manufactured AlSi10Mg Using Friction Stir Processing, *Corros. Sci.*, 2021, **178**, p 109073
22. W.T. Read and W. Shockley, Dislocation Models of Crystal Grain Boundaries, *Phys. Rev. APS*, 1950, **78**(3), p 275
23. H. Luo, X. Wang, C. Dong, K. Xiao, and X. Li, Effect of Cold Deformation on the Corrosion Behaviour of UNS S31803 Duplex Stainless Steel in Simulated Concrete Pore Solution, *Corros. Sci.*, 2017, **124**, p 178–192